nanomaterials

MDPI

Article

Enhanced NH_3 Sensing Performance of Mo Cluster-MoS_2 Nanocomposite Thin Films via the Sulfurization of Mo_6 Cluster Iodides Precursor

Meiqi Zhang [1,2,3], Fabien Grasset [3,4,*], Yuji Masubuchi [1,5], Toshihiro Shimada [1,5], Thi Kim Ngan Nguyen [3,6], Noée Dumait [4], Adèle Renaud [4], Stéphane Cordier [4], David Berthebaud [3], Jean-François Halet [3] and Tetsuo Uchikoshi [1,2,3,*]

1 Graduate School of Chemical Sciences and Engineering, Hokkaido University, Kita 13 Nishi 8, Kita-ku, Sapporo 060-8628, Japan
2 Research Center for Functional Materials, National Institute for Materials Science, 1-2-1 Sengen, Tsukuba 305-0047, Japan
3 CNRS–Saint-Gobain–NIMS, IRL3629, Laboratory for Innovative Key Materials and Structures (LINK), National Institute for Materials Science, 1-1 Namiki, Tsukuba 305-0044, Japan
4 Univ Rennes, CNRS, Institut des Sciences Chimiques de Rennes (ISCR)–UMR 6226, F-35000 Rennes, France
5 Division of Applied Chemistry, Faculty of Engineering, Hokkaido University, Kita 13 Nishi 8, Kita-ku, Sapporo 060-8628, Japan
6 International Center for Young Scientists, ICYS-SENGEN, Global Networking Division, National Institute for Materials Science, 1-2-1 Sengen, Tsukuba 305-0047, Japan
* Correspondence: fabien.grasset@univ-rennes1.fr (F.G.); uchikoshi.tetsuo@nims.go.jp (T.U.)

Abstract: The high-performance defect-rich MoS_2 dominated by sulfur vacancies as well as Mo-rich environments have been extensively studied in many fields, such as nitrogen reduction reactions, hydrogen evolution reactions, as well as sensing devices for NH_3, which are attributed to the under-coordinated Mo atoms playing a significant role as catalytic sites in the defect area. In this study, the Mo cluster-MoS_2 composite was creatively synthesized through a one-step sulfurization process via H_2/H_2S gas flow. The Mo_6 cluster iodides (MIs) coated on the fluorine-doped tin oxide (FTO) glass substrate via the electrophoretic deposition method (i.e., MI@FTO) were used as a precursor to form a thin-film nanocomposite. Investigations into the structure, reaction mechanism, and NH_3 gas sensing performance were carried out in detail. The results indicated that during the gas flowing, the decomposed Mo_6 cluster iodides played the role of template and precursor, forming complicated Mo cluster compounds and eventually producing MoS_2. These Mo cluster-MoS_2 thin-film nanocomposites were fabricated and applied as gas sensors for the first time. It turns out that after the sulfurization process, the response of MI@FTO for NH_3 gas increased three times while showing conversion from p-type to n-type semiconductor, which enhances their possibilities for future device applications.

Keywords: molybdenum octahedral cluster; molybdenum disulfide; sulfurization process; gas sensor

Citation: Zhang, M.; Grasset, F.; Masubuchi, Y.; Shimada, T.; Nguyen, T.K.N.; Dumait, N.; Renaud, A.; Cordier, S.; Berthebaud, D.; Halet, J.-F.; et al. Enhanced NH_3 Sensing Performance of Mo Cluster-MoS_2 Nanocomposite Thin Films via the Sulfurization of Mo_6 Cluster Iodides Precursor. *Nanomaterials* **2023**, *13*, 478. https://doi.org/10.3390/nano13030478

Academic Editors: Alexander Kromka and Antonella Macagnano

Received: 30 November 2022
Revised: 16 January 2023
Accepted: 18 January 2023
Published: 24 January 2023

1. Introduction

Graphene-like molybdenum disulfide (MoS_2), with its well-known two-dimensional (2D) layered "sandwich" structure, has attracted significant attention over the years due to its unique electronic, optical, and chemical properties [1–4], which can be exploited in transistors [5,6], solar cells [7,8], catalysts [9–11], and sensors [12–14]. In this "sandwich" structure, one layer of molybdenum atoms is sandwiched between two layers of sulfur atoms. In the domain of catalysis, such MoS_2 three-layer structures have been widely investigated for their catalytic activity, which is strongly dependent on the edge sites [15]. To enhance the catalytic performance, researchers studied the synthesis of defect-rich MoS_2, in which a sulfur vacancy that created the edge sites plays an important role [16–18]. Indeed,

at the sulfur vacancy sites, the surrounding under-coordinated Mo atoms introduce gap states that facilitate N_2 absorption or hydrogen bonding, which improves the performance of the nitrogen reduction reaction (NRR) [19], hydrogen evolution reaction (HER) [20,21], as well as sensing [22–24].

With the development of defect engineering, researchers have devoted themselves to the synthesis of S vacancies defect-rich MoS_2 by using the hydrothermal route [25,26] and the chemical vapor deposition (CVD) method [27], which can control the sulfur-molybdenum ratio during the reaction to create defects. Alternatively, 2D-MoS_2 decorated with Mo clusters has started to attract some attention as a catalyst for the generation of acetylene via the CO hydrogenation reaction [28]. A higher electrocatalytic NRR activity has been theoretically proposed using Mo_x clusters (x = 1~11) supported on MoS_2 [29]. Moreover, Jin et al. demonstrated the in situ fabrication of Mo_6S_6-nanowire-terminated edges in the monolayer MoS_2 [30] and developed a mass transport method for the formation of Mo chains induced by Mo clusters along the sulfur vacancy lines, aimed at tuning the defects and, thus, the materials' structure–property relationship in a well-controlled manner [31]. However, only a few studies have been conducted to generate MoS_2 by sulfuring chalcogenide clusters, such as $Mo_6S_2I_8$, as precursors [32,33].

In this study, we creatively pioneered the efficient synthesis route of Mo cluster-MoS_2 thin-film nanocomposites by a sulfurization process using Mo_6 cluster iodides as the precursors. Mo_6 cluster units are inorganic molecules containing six Mo atoms forming an octahedral skeleton that are connected by direct metal–metal bonds and are bonded with organic or inorganic ligands to stabilize the metal core. The interest in Mo_6 clusters-based compounds started with the discovery of the superconductivity in the Chevrel phases [34]. In recent decades, the optical properties and the chemical activity of Mo_6 clusters derived from their unique electronic structure [35–37] have been investigated and developed in many fields [38], such as luminescent [39–41], energy [42], and catalysis applications [43]. Among them, Nguyen et al. successfully developed a general process to coat metal-cluster-unit-based thin films, for example, Mo_6 cluster iodides ($Cs_2Mo_6I_{14}$, CMI; more specifically, $Cs^+_2[\{Mo_6I^i_8\}I^a_6]^{2-}$, where i and a represent the inner and apical iodide ligands, respectively, that surround the Mo_6 octahedra) on a fluorine-doped tin oxide (SnO_2:F, FTO) glass substrate by the electrophoretic deposition (EPD) method [44]. This EPD method maintained the optoelectronic properties of the initial CMI raw powder, which will significantly promote the fabrication of Mo_6-cluster-based optoelectronic devices in the future. Moreover, Renaud et al. recently proved that the Mo_6 cluster iodides are a new class of ambipolar materials [45], and the $\{Mo_6I^i_8\}$-based thin films (noted MI@FTO) fabricated via the EPD method have shown a significant application potential as a photoabsorber in an all-solid solar cell in the future. Moreover, Guy et al. used various Mo_6 clusters powders ($Cs_2Mo_6CI_{14}$, $(TBA)_2Mo_6Br_{14}$, etc.) as precursors to synthesize Mo_xN_y nanomaterials with different compositions (Mo_2N and Mo_5N_6) [46]. In contrast to the conventional synthesis using MoO_3 as a precursor, these Mo_xN_y products were prepared at lower temperatures and showed significant catalytic performances for the water–gas shift reaction.

In a previous study, we successfully produced MoS_2 from Mo_6Br_{12} powder as a precursor via two sulfurization processes [47]. Using the gas flow method, the sulfurization reaction occurred at 250 °C, but the product was a micron-sized amorphous MoS_2 powder. This reaction process still needs to be developed and the reaction mechanism better understood. Therefore, in this study, we decided to use this gas flow method combined with the EPD technology to establish a one-step sulfurization method at low temperature to fabricate a Mo cluster–MoS_2 thin film nanocomposite by using pre-prepared MI@FTO coatings as the precursor. The morphology and the reaction mechanism were investigated in detail. For future device applications, the obtained thin-film samples were carefully evaluated for their NH_3 gas sensing performance. The main results are reported and discussed.

2. Materials and Methods

2.1. Chemicals

The synthesis path of the $Cs_2Mo_6I_{14}$ initial powders via the solid-state method [48,49] and the MI@FTO films fabricated by using the EPD method [50] have been well established in our previous studies.

Briefly, $Cs_2Mo_6I_{14}$ was synthesized by reacting CsI and MoI_2 mixed and heated at 700 °C for 4 days in a silica tube sealed under vacuum. For the EPD process, the $Cs_2Mo_6I_{14}$ raw powder was dissolved in acetone (reagent-grade chemicals, 99.5%) at the concentration of 5 g per liter. The solution was then filtered using a 0.2 μm filter to remove any insoluble impurities. At the same time, the FTO glass substrate (Kenis Corp., Osaka, Japan) was cut into a 25 mm × 10 mm piece and washed in detergent and acetone for 30 min in an ultrasonic bath. Finally, the FTO substrate was used as the anode and immersed in a $Cs_2Mo_6I_{14}$ cluster solution. The coating process was performed at 10 V for 5 min. Cs^+ cations and $[\{Mo_6I^i_8\}X^a_6]^{2-}$ (X = I, OH) were deposited on the cathode and the FTO glass anode, respectively [45]. It should be noted that during the EPD coating process, the $[\{Mo_6I^i_8\}I^a_6]^{2-}$ cluster molecules will lose two iodide apical ligands, which were replaced by water ligands, as confirmed by the XPS result in a previously published report [45]. Accordingly, the final composition of the MI@FTO film in this study is described as $[\{Mo_6I^i_8\}I^a_4(H_2O)^a_2]\cdot xH_2O$. The MI@FTO thin films deposited on the FTO substrate were used for the sulfurization process.

2.2. Sulfurization Process

All the sulfurization reactions were carried out in a tubular furnace with a flowing H_2/H_2S (90%/10%) mixture gas (99.9%, Air Liquid). The MI@FTO sample was initially placed in an aluminum boat, then into the furnace. The reaction chamber was purged with N_2 gas for 30 min before the start of the reaction to ensure removal of the air, and the furnace was always at 1 atmospheric pressure. The H_2/H_2S gas was then introduced at the rate of 15 mL/min in the temperature range of 250–450 °C, and the main reaction time was 1 h for all the MI@FTO films with the increasing rate of 5 degrees per minute. The H_2S acted as the sulfur source for the sulfurization reaction and the H_2 acted as the reducing atmosphere to protect the cluster film from oxidation. An illustration of the EPD and the sulfurization process for the MI@FTO is shown in Figure 1a. According to the reaction temperature, the final products were denoted as MI-250, MI-300, etc. The reaction time was labeled for the specific sample, which is the extended reaction times, e.g., MI-350-3h.

2.3. Fabrication and Measurement of Gas Sensor

The fabrication and measurement of the MI@FTO gas sensor are illustrated in Figure 1b. This measurement was conducted by a chemiresistive gas sensor, which consisted of two electrodes connected to the sensing material. The change in resistance or current of the sensor device was measured in order to analyze the concentration of the target gas.

First, a 46 μm Au wire covered the MI@FTO surface, and the covered area was used for the performance measurement. An approximately 50 nm Au layer was deposited on the exposed sample surface by a vacuum evaporator (VG Microtech E6700S, Newhaven, UK) to improve the surface conductivity. A Cu wire was connected from the Au-deposited area to the ampere-meter (Graphtec midi Logger GL240, Graphtec Corporation, Yokohama, Japan) to monitor and record the real-time current. The MI@FTO was placed in an alumina tube with flowing NH_3 gas (99.9%, Sumitomo Seika Chemicals, Tokyo, Japan) for the measurements.

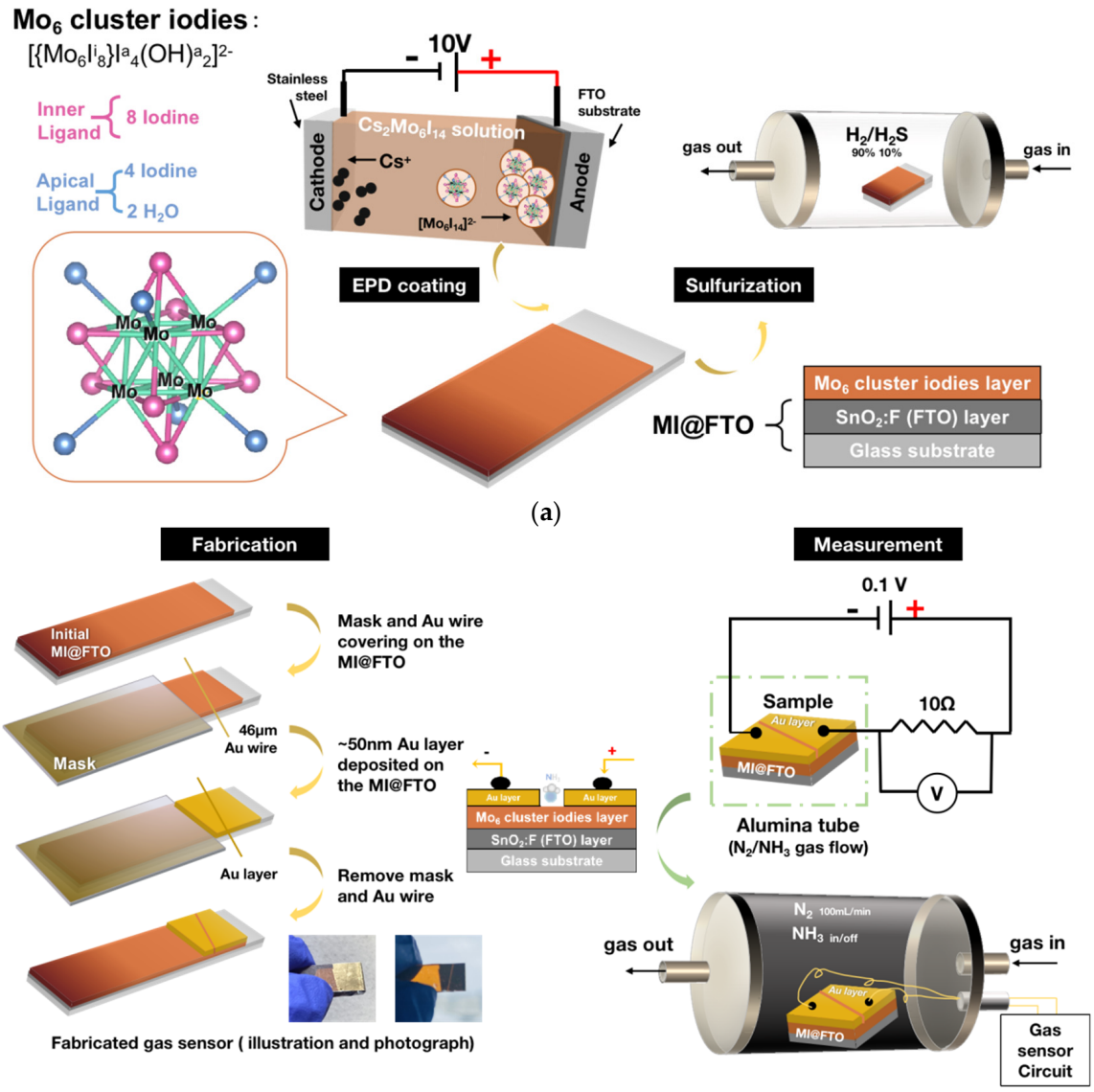

Figure 1. (**a**) Illustration of MI@FTO prepared via EPD and sulfurization processes. (**b**) Illustration of the gas sensor fabrication and measurement.

2.4. Characterization

The structure and morphology of the thin-film samples, before and after sulfurization, were investigated by the grazing-incidence X-ray diffraction technique (GIXRD, SmartLab, Rigaku Corp., Tokyo, Japan) at room temperature using Cu Kα radiation (λ = 1.5406 Å) at 50 mA and 40 kV power, and the incident beam was set at fixed critical w angles ($0.2° \leq w \leq 0.8°$). The layered structures were analyzed by micro-Raman spectroscopy (HORIBA T64000, Kyoto, Japan) using a 515 nm laser source. The surface morphology and the elemental composition mapping of the thin-film sample were analyzed by field emission scanning electron microscopy (FE-SEM, Hitachi SU4800, Tokyo, Japan) at 10–15 kV coupled with an energy-dispersive X-ray (EDX) analysis device, and high-resolution observations of the powder scratched from the thin-film sample were performed by a high-resolution transmission electron microscope (HRTEM, JEOL 2100F, Tokyo, Japan) equipped with an EDX analysis device. The electron binding energy spectra of the thin-film samples were measured by X-ray photoelectron spectroscopy (XPS, ULVAC Quantum-2000, Chigasaki, Japan) using Al Kα radiation at 15 kV and 50 W and a take-off angle of 45°. All the binding energies were calibrated versus the C 1s peak of the adventitious carbon at 285 eV.

3. Results and Discussion

3.1. Structure and Morphology

The GIXRD results in Figure 2a show the patterns of the initial MI@FTO and sulfurized samples. The wide peak observed around 9–12 degrees and the sharp crystal peaks at the higher 2θ angle in the initial MI@FTO pattern can be identified as the amorphous Mo_6 cluster iodide film and SnO_2:F from the FTO substrate, respectively, which is consistent with our previous studies [45,51]. MoS_2 and SnS are found as the final products during this sulfurization process (see MI-450 pattern in Figure 2a). Indeed, MoS_2 is the final product of the sulfurization reaction starting from the MI@FTO thin-film precursor occurring from 250 °C, and this result is consistent with the powdered Mo_6Br_{12} cluster precursor [47]. The wide peak initially measured around 9–12 degrees, due to the Mo_6 cluster iodides, has shifted to 14 degrees upon increasing the temperature. This indicates that the Mo_6 cluster iodide has entirely disappeared in favor of MoS_2. The presence of SnS crystals over 350 °C is unexpected. The SnO_2 layer between the Mo_6 cluster iodides and the SiO_2 glass layer plays the role of the Sn source leading to SnS crystals at the end of the process. The pattern of MI-300 shows complex peaks of multiple phases. Considering that SnO_2 may have been involved in the reaction, the product might contain the Mo_xS_y complex [52], the Sn_xS_y complexes [53], and also the Sn-Mo cluster complexes [54]. Additionally, the involvement of an O source derived from SnO_2 may also have contributed to the formation of metal oxysulfide complexes [55]. In general, the FTO substrates are used as substrates for the synthesis of tin sulfides using the CVD method because the SnO_2 surface is suitable for the growth of tin sulfides and does not participate in the reaction at such temperatures [56,57]. This fact implies that the excellent catalytic properties of the Mo_6 cluster iodides promote the SnO_2 layer in order to participate in the sulfurization reaction [57].

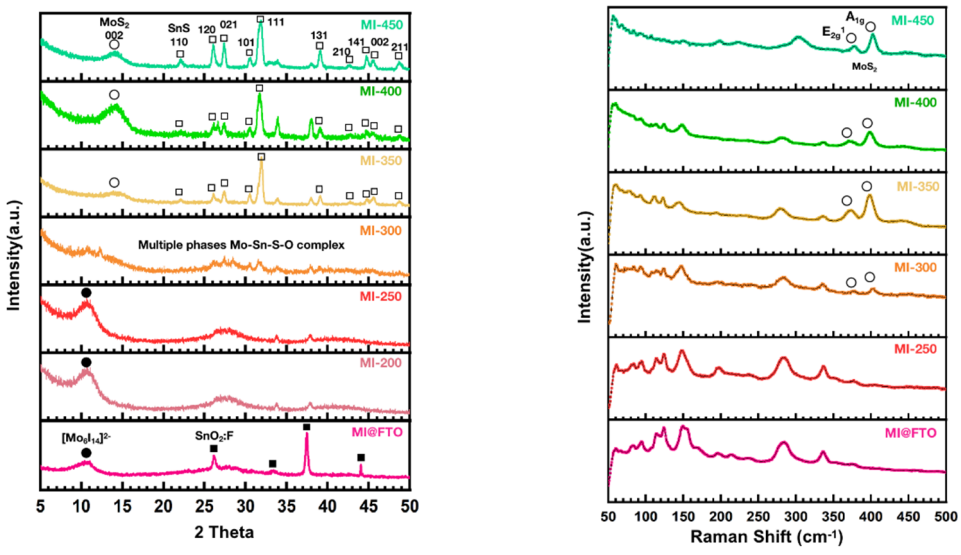

Figure 2. (**a**) GIXRD pattern of MI@FTO and sulfurized samples at different temperatures; (**b**) Raman spectra of MI@FTO and sulfurized samples under 515 nm excitation.

In contrast to the well-grown SnS crystal, the final product of the reaction, only one wide diffraction pattern present in the XRD patterns was used to confirm the formation of MoS_2. In the Raman spectrum (see Figure 2b), the MoS_2 layered structure peaks are observed around 375 cm^{-1} and 400 cm^{-1}, which represent the in-plane vibration ($E_{2g}{}^1$) and out-of-plane vibration (A_{1g}), respectively, beyond 300 °C. It is indicated that the Mo_6 cluster iodides, used as a precursor, are gradually sulfurized into the layered MoS_2 structure, which is consistent with the wide peak around 14 degrees corresponding to the MoS_2 (002) surface in the XRD pattern.

Figure 3a shows pictures of the initial MI@FTO and sulfurized samples at different temperatures. The initial MI@FTO film is a translucent orange film. During the sulfurization process, the color of the MI@FTO films undergo a change from orange to dark brown (MI-250) to dark gray with a metallic luster (from MI-300 to MI-450), which indicates that the sulfurization reaction occurs beyond 250 °C. The dark gray color of the metallic luster sample must also correspond to the MoS_2 and SnS phases. The surface morphology of the initial MI@FTO observed by FE-SEM and illustrated in Figure 3b shows isolated $[\{Mo_6I^i_8\}X^a_6]^{2-}$ (X = I, OH) nanoparticles with diameters around 20–50 nm up to 300 °C. As the temperature increases to 350 °C, the nanoparticles are sintered into a continuous porous structure.

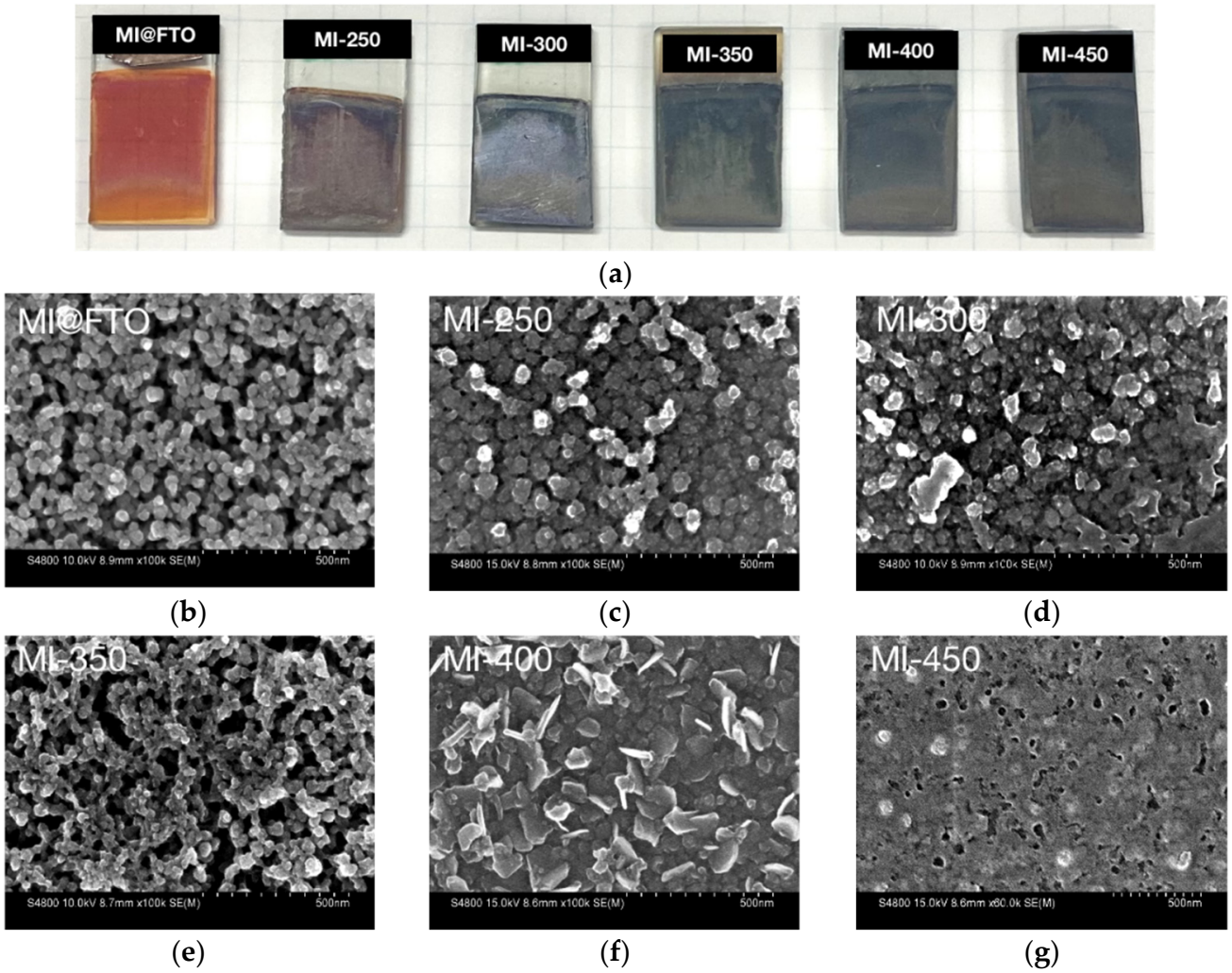

Figure 3. Pictures and FE-SEM observation with the scale bar at 500 nm of MI@FTO and sulfurized samples: (**a**) photographs of samples on a squared paper (5 mm × 5 mm); (**b**) initial MI@FTO; (**c**) MI-250; (**d**) MI-300; (**e**) MI-350; (**f**) MI-400; (**g**) MI-450.

At 400 °C, the surface morphology becomes nanoflaked with a surface area around 100 nm^2. At the same time, the isolated bulk crystal around 500 nm in size is also observed on the surface, as shown in Figure 4a,b. When the temperature increases to 450 °C, the surface becomes bumpy. Isolated crystals and cracks can also be observed on the surface, as shown in Figure 4c,d.

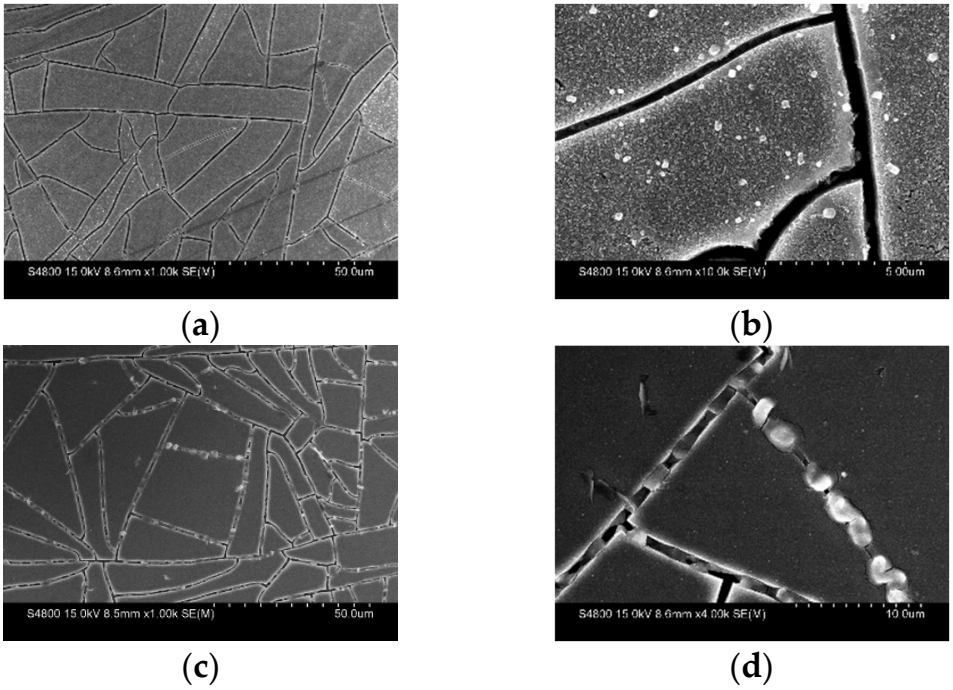

Figure 4. SEM observation of (**a**) MI-400 with the scale bar at 50 μm; (**b**) MI-400 with the scale bar at 5 μm; (**c**) MI-450 with the scale bar at 50 μm; (**d**) MI-450 with the scale bar at 10 μm.

These results illustrate that there are two reactions occurring during the sulfurization of MI@FTO, i.e., one starting at 250 °C, when the Mo_6 clusters are sulfurized, leading to MoS_2; one starting at 350 °C, not only when the Mo_6 cluster sulfurization reaction occurs, but also when the Mo_6 clusters catalyze the sulfurization of SnO_2 into SnS.

3.2. Mechanism of the MI@FTO Sulfurized into MoS_2 and SnS crystal Growth Hypothesis

In order to clarify the sulfurization mechanism of the Mo_6 cluster iodides, the MI-250 powder samples were scratched from the films for HRTEM observations (see Figure 5) in order to exclude interference from the FTO substrate and provide an easy sample preparation.

It is noteworthy that the EDX analysis in Figure 5a demonstrates that the MI-250 contains Mo, S, O, and I elements, but not the Sn element, which means that SnO_2 is not involved in the reaction below 250 °C. The high-resolution analysis of the O element in the nanoparticle revealed that the Mo is oxidized. In addition to the MoS_2 layer structure, the MoO_3 crystal structure is also observed in Figure 5b. Moreover, the electron energy loss spectroscopy (EELS) analysis in Figure 5c revealed that there is a high concentration of Mo and S elements in the shell of the MI-250 nanoparticles but just a little oxygen. Conversely, the core contains a small amount of S and a high concentration of the Mo and O elements. This fact shows that, first, the film-bound water during the EPD process [45,58] serves as the O source, suggesting that the initial Mo_6 cluster iodide is probably oxidized into MoO_3. The H_2S gas then serves as the S source for the subsequent sulfurization to produce MoS_2 on the nanoparticle surface.

It has been reported that MoO_3 can play the role of a precursor on the FTO substrates at low temperatures to be sulfurized into MoS_2. On the other hand, SnO_2 in the FTO coating is stable and does not participate in the reaction even when the temperature increases to 700 °C; thus, the final product, the MoS_2 sulfurized from the MoO_3 precursor, would not contain SnS. [59]. This fact confirms that the MoO_3 used as a mid-product in this study is not the key material that catalyzes the SnO_2:F layer on the FTO substrate to generate SnS under the H_2/H_2S.

Our study is the first report showing that Mo_6 cluster iodides deposited on FTO substrates can generate SnS at 350 °C without external Sn sources, indicating that the Mo_6

cluster iodides have a catalytic role. Although the reaction mechanism is still unclear, we attempted to provide some explanations for the growth of the SnS crystals. Figure 6a shows the FE-SEM observation focusing on the crack of the thin-film samples at different temperatures. The main morphology starting from the Mo_6 cluster iodide nanoparticles is consistent with the observation shown in Figure 3. At high temperatures, cracks inevitably occur in the MI@FTO films, and the appearance of the cracks exposes the SnO_2 layer to the H_2/H_2S gas flow and concomitantly to the Mo_6-cluster-iodide-based layer. Multiple SnS_x phases are observed by heating of the blank FTO, free of Mo_6 cluster iodides, starting from 350 °C (see Figure S1). However, the SnS crystals grow well from the exposed SnO_2 surface and are catalyzed by the Mo_6 cluster iodides at MI-350, and MI-400 also shows the bulk SnS crystal around 500 nm.

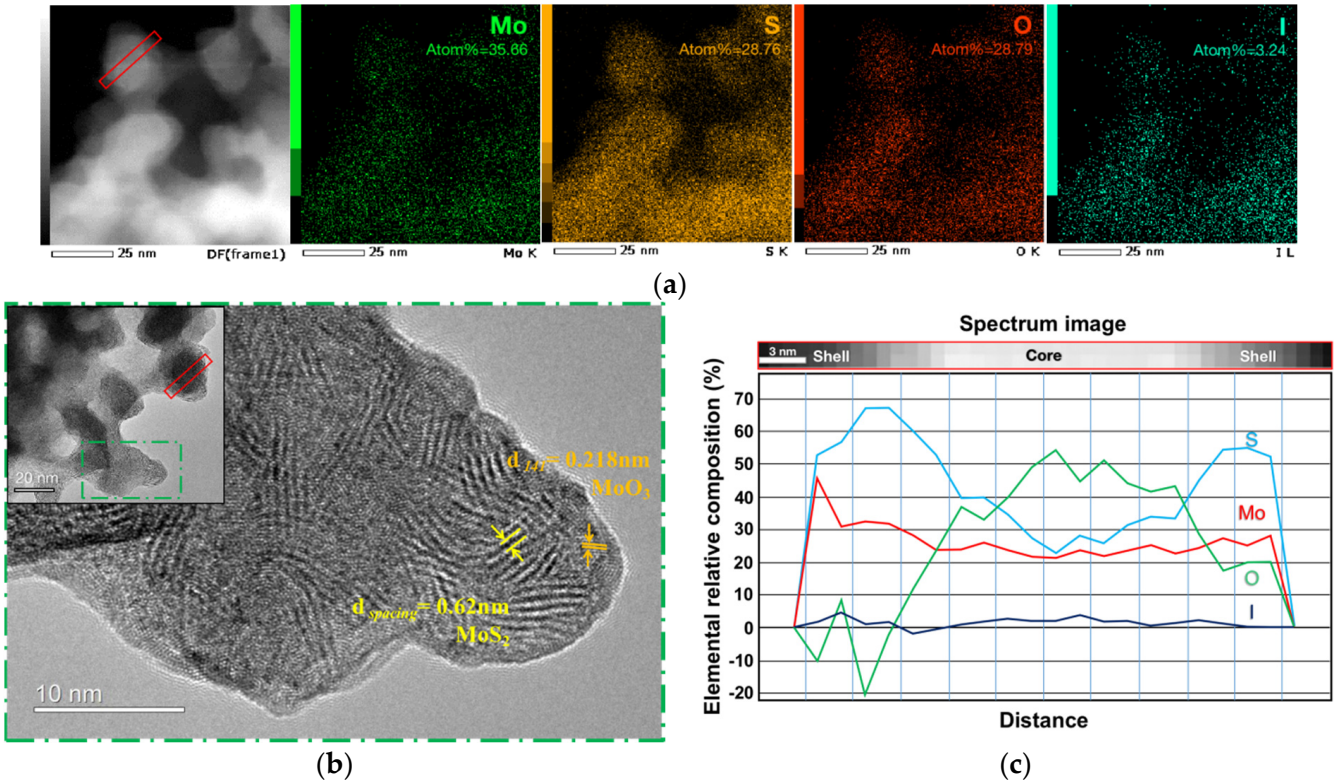

Figure 5. HRTEM observation of MI-250 powder scratched from thin films with the same observation area is marked in the figure. (**a**) Element mapping from HRTEM equipped with EDX device with the scale bar at 25 nm, and the elemental quantitative result is marked; (**b**) HRTEM image of MI-250; (**c**) EELS analysis of the MI-250 nanoparticles.

Based on this result, we extended the sulfurization time to 3 h (i.e., MI-350-3h), and the morphology of MI-350-3h still retains the shape of the nanoparticles with a diameter of about 50 nm, but these particles are sintered together. Figure 6b shows a cross-section of the MI-350-3h film sample with the presence of Sn that highlights the migration of the Sn in the Mo layer and a very uniform doping. This indicates that the SnO_2 layer reacts with the Mo_6 cluster iodide along the layer, not only on the top surface.

The MI-350-3h powder samples were also scratched from the films for the HRTEM observations (see Figure 7). The layer spacing of the 2D structure is 0.65 nm, which is consistent with MoS_2. In addition, the lattice spacing of the nanocrystal structure is 0.28 nm, which is consistent with the (111) plane of SnS from the XRD results. The element mapping clearly shows the uniform distribution of the Mo, Sn, and S elements in the sample.

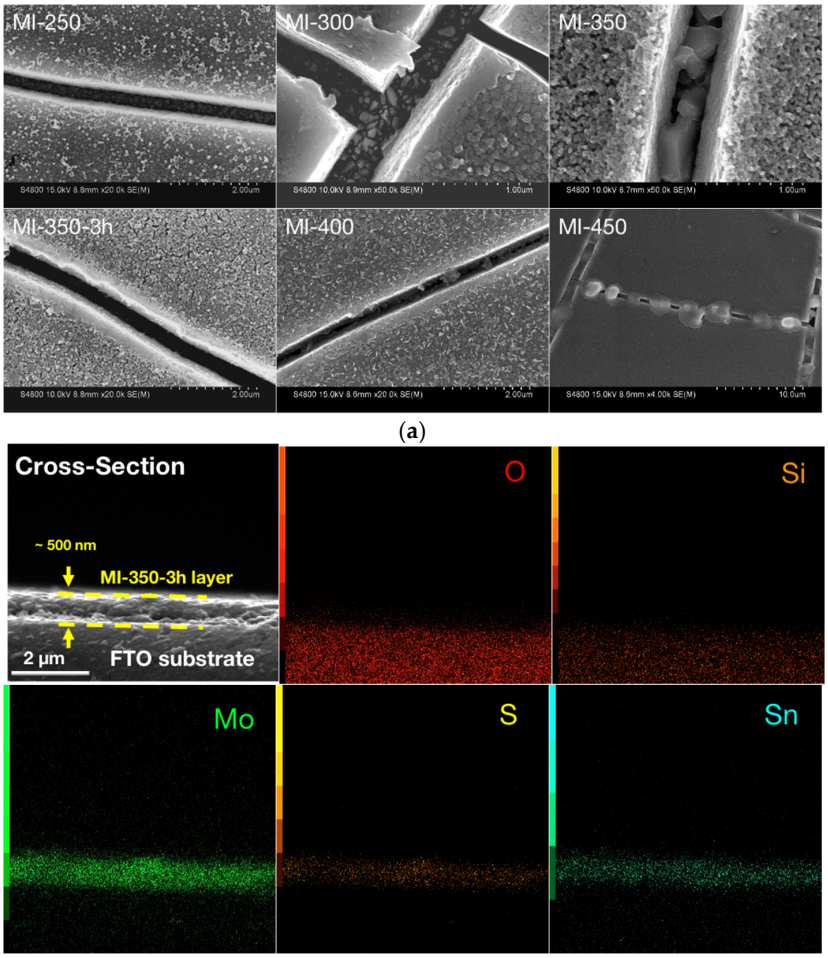

Figure 6. SEM observation of thin-film samples: (**a**) the cracks and (**b**) the cross-section of MI-350-3h.

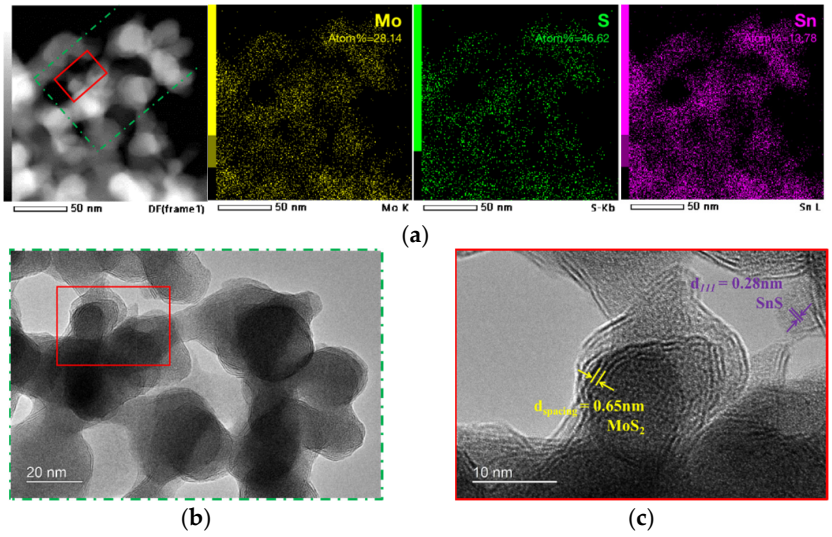

Figure 7. HRTEM observation of MI-350-3h powder scratched from thin film; the same observation area is marked in the figure. (**a**) Element mapping from HRTEM equipped with EDX device with the scale bar at 50 nm, and the elemental quantitative result is marked; (**b**) HRTEM image of MI-350-3h with the scale bar at 20 nm; (**c**) scale bar at 10 nm.

It is noteworthy that the EDX elemental quantitative analysis result shows that the content of the I element in MI-350-3h is I% = 0.07, while in the MI-250 sample, I% = 3.24. The content of the I element is much lower than those of the Mo and S elements in the sulfurized MI@FTO sample as the sulfur replaces the iodine ligand in the Mo_6 cluster unit to form the Mo_xS_y cluster. The Mo cluster structure gradually decomposes to form MoS_2, which is the final product. The I_2 gas generated by the decomposed Mo_x ($1 \leq x \leq 6$) cluster iodides reacts with H_2/H_2S and leaves the reaction chamber as a by-product in the gas flow. The Mo_6 cluster iodides and I_2 gas by-product during decomposition of the Mo_x cluster ($1 \leq x \leq 6$) may play an important role here to catalyze the SnO_2:F layer to the SnS crystal.

The generation of halogen gas by-products during the sulfurization of the Mo_6 clusters has also been reported in our previous studies [47]. By using the chemical vapor transport (CVT) method, the Mo_6Br_{12} and sulfur powder were mixed and sealed in a quartz vacuum tube for the sulfurization reaction; the Br_2 gas and $MoBr_3$ by-product are retained in the tube and affects the pressure of the vacuum tube reaction system, which affects the final product, MoS_2, as a 3D-formed nanosheet or single crystal.

Figure 8 shows the XPS results of four thin-film samples, i.e., MI@FTO, MI-250, MI-350, and MI-350-3h. One Mo $3d_{5/2}$-$3d_{3/2}$ doublet peak is identified in the Mo 3d spectrum for the initial MI@FTO with binding energies of 229.3 eV–232.4 eV, suggesting the Mo^{4+} states. Moreover, two I $3d_{5/2}$-$3d_{3/2}$ doublet peaks in the I 3d spectrum with a ratio of 2:1 are observed, which is consistent with our earlier research and correspond to the ratio of the inner ligands to apical ligands in the $[\{Mo_6I^i_8\}I^a_4(H_2O)^a_2]$ cluster molecular structure combining H_2O molecules [45,60]. Three Mo $3d_{5/2}$-$3d_{3/2}$ doublet peaks are attributed to the Mo^{4+}, Mo^{5+}, and Mo^{6+} states for MI-250. According to the HRTEM result of MI-250, the Mo^{4+} states can be attributed to the MoS_2 layered structure, whereas the Mo^{5+} states correspond to the Mo_xS_y clusters [61–64]. Finally, the Mo^{6+} doublet peak must be due to MoO_x, which is produced from the MI@FTO and bound water. Two doublet peaks are observed in the MI-250 I 3d spectrum with a ratio of roughly 1:1. The presence of the I 3d peak is not only consistent with the EDX elemental quantitative analysis result of the MI-250 sample (see Figure 5a), but the two doublet peaks representing the inner ligand and apical ligand also suggest that MI-250 contains a minor amount of molybdenum iodide sulfide clusters [65]. The three S $2p_{3/2}$-$2p_{1/2}$ doublet peaks present in the MI-250 S 2p spectrum should all belong to the Mo-S compounds because MI-250 is devoid of Sn. The terminal S^{2-} in MoS_2 is indicated by a major doublet at the binding energies of 162.1 eV–163.3 eV. On the other hand, a minor doublet is assigned to the apical/bridge S at the slightly higher binding energies of 162.9 eV–164.2 eV, which belong to the Mo_xS_y phase with the Mo^{5+} state. An additional terminal S^{2-} doublet peak is also recognized as a minor doublet observed at the lower binding energies of 161.2 eV–162.4 eV. These low-binding energies are caused by the effect of H_2 during the synthesis [66].

In the MI-350 and MI-350-3h samples, no Mo^{6+} state, representing MoO_x, is found in the Mo 3d spectrum. The I 3d peak also disappears, proving that MoO_x as an intermediate product is completely sulfurized. The content of the Mo^{5+} ions in the product significantly decreases when the sulfurization time increases from 1 to 3 h, demonstrating that the Mo_xS_y cluster phase gradually produces MoS_2 that is compatible with the Raman results.

Two Sn 3d $3d_{5/2}$-$3d_{3/2}$ doublet peaks are observed in the Sn 3d spectrum of MI-350 and MI-350-3h, suggesting the Sn^{4+} and Sn^{2+} states. Sn^{4+} is associated with the Sn-doping into the MoS_2 complex and the SnO_2 substrate combined with the HRTEM results obtained for MI-350-3h, whereas the Sn^{2+} state corresponds to the SnS crystals. In the S 2p spectrum, the doublet peak corresponds to the Sn-S bonds. These results demonstrate that the SnO_2-coated layer in the FTO substrate begins to take part in the reaction and synthesizes SnS, which is consistent with the XRD results, in which the Mo_6 clusters demonstrate their outstanding catalytic capabilities.

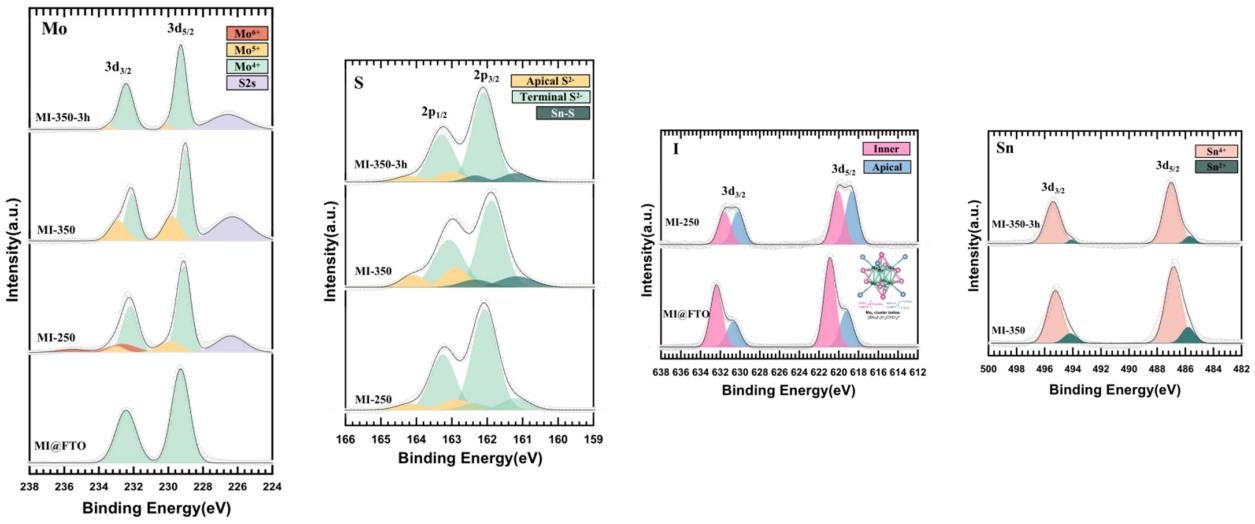

Figure 8. XPS result of MI@FTO, MI-250, MI-350, and MI-350-3h thin films: (**a**) Mo 3d spectrum; (**b**) S 2p spectrum; (**c**) I 3d spectrum; (**d**) Sn 3d spectrum.

Based on this result, the sulfurization reaction of the Mo_6 cluster iodide thin films can be described as follows: first, the Mo_6 clusters acquire bound water during the EPD coating, and the bound water reacts with the Mo_6 cluster iodides at 250 °C to form MoO_x; subsequently, MoO_x is sulfurized into MoS_2 by H_2S. In this process, the iodide ligand is gradually replaced by sulfur ligands and the Mo_6 clusters are gradually decomposed. When the reaction temperature becomes higher or the reaction time becomes longer, the final product is the layered MoS_2. Thus, the composition of the MI-250 thin film should be the MoO_x-Mo_xS_y cluster-MoS_2 composite with doped iodide.

On the other hand, the main component of MI-300 should be a metal sulfide (oxysulfide) complex of Mo and Sn, while the components of MI-350 and MI-350-3h should be SnS-MoS_2 nanoparticles. The MI-350-3h thin film has a porous sintered particles morphology. The distribution of the Mo and Sn elements is, thus, uniform, which is obtained at such a low synthesis temperature. Although the reaction mechanism of SnO_2 catalyzed by Mo_6 cluster iodides to form SnS is not known, it is worth further research.

3.3. NH_3 Sensor Application

Ligated Mo_6-cluster-containing compounds used for sensing activity are currently limited to oxygen sensor [67,68], pH sensing [69], biological sensing [70], and photo-response [58,71]. According to theoretical calculations, such compounds are predicted to have a good selectivity for NH_3 in the NRR [29]. Previous studies have also demonstrated that they exhibit a photo-response and can react with NH_3 to form Mo_xN_y species at 400 °C [46,58,71]. Thus, we inferred that Mo_6 cluster iodides should have a specific adsorption of NH_3 even at room temperature and that this adsorption could cause a potential change when a voltage is applied to the MI@FTO, which was proved to be an ambipolar material (E_g = 1.9 eV). In addition, the nanoparticle morphology of the material could also increase the specific surface area and, thus, enhance the adsorption effect. Based on these facts, a simple MI@FTO sensor was designed and fabricated to verify this hypothesis (see Figure 1b).

The MI@FTO and sulfurized sample gas sensors were carefully tested at room temperature, 1 atmosphere, and in shaded light in order to investigate the sensing performance of NH_3 under a N_2 atmosphere for its potential applications in gas detection. The flow rate of the N_2 gas stream was constant at 100 sccm. The flow rate of the NH_3 gas was adjusted to achieve a change in the concentration of NH_3 in the atmosphere. Its real-time current

change was detected with the voltage of 0.1 V by flowing NH_3 gas in the alumina tube. The gas sensing response (%) was calculated using the following equation:

$$\text{Response}(\%) = \frac{|I_g - I_0|}{I_0} \times 100\% = \frac{\Delta I}{I_0} \times 100\% \quad (1)$$

where I_0 is the base current, and I_g refers to the corresponding current with the NH_3 gas *exposure*.

Figure 9a shows the result of the NH_3 sensing performance of the initial MI@FTO and MI-250 samples. The initial MI@FTO with the pure Mo_6 cluster iodide film was, for the first time, used as a gas sensor and demonstrated a significant responsiveness. Gas sensing mechanisms can be interpreted as electron (or hole) transport between a sensing film and the target gas via charge transfer. Depending on whether the gas is oxidizing or reducing (e.g., NH_3) and the sensing film is a p- or n-type semiconductor, electrons are withdrawn from or donated to the sensing film, which would cause the resistance of the sensing material to increase or decrease [72–74]. The initial MI@FTO shows an increased resistance when exposed to NH_3 gas, while MI-250 shows a decrease in resistance, proving that MI@FTO shows the behavior of a p-type semiconductor, while MI-250 is an n-type conductor (see Figure 9e). This conversion could be the result of a sulfur defect and iodine doping [75–77].

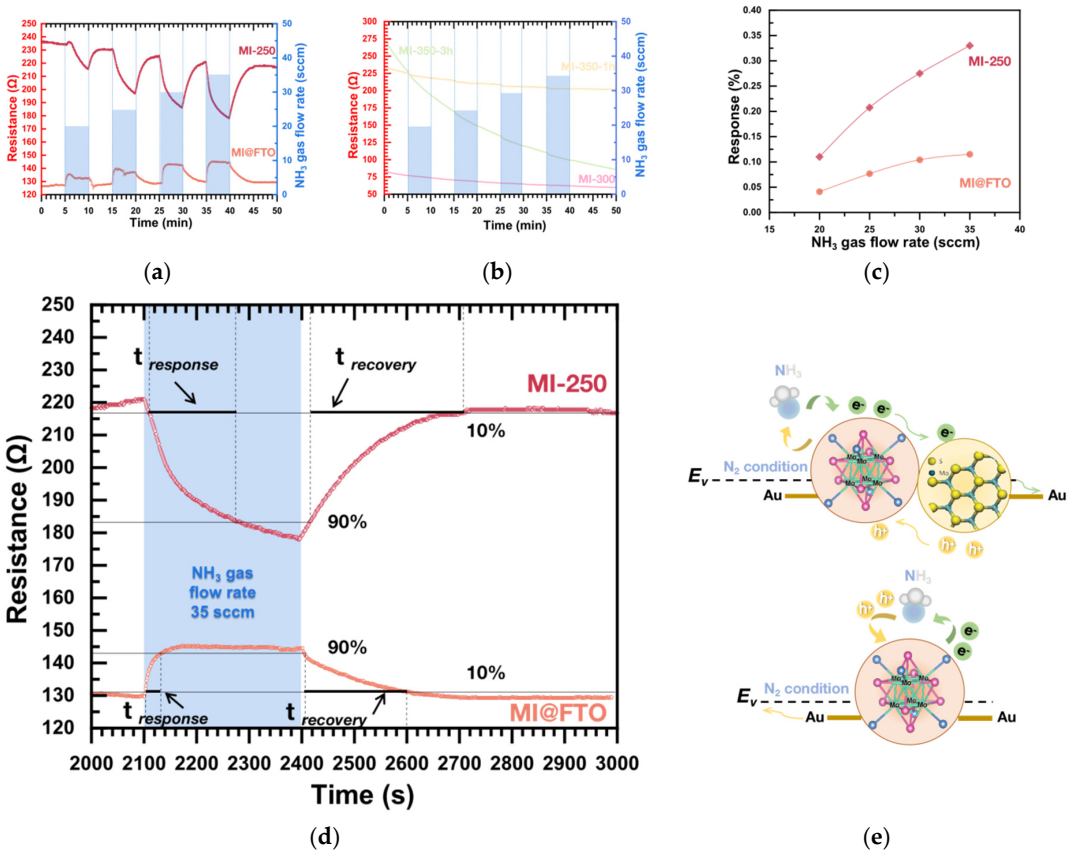

Figure 9. NH_3 sensing performance of (**a**) MI@FTO, MI-250; (**b**) MI-300, MI-350, and MI-350-3h thin films; (**c**) calculated response of the MI@FTO and MI-250 gas sensor corresponding to gas flow rate of NH3; (**d**) transient response and recovery times of NH_3 (35 sccm) for MI@FTO and MI-250 gas sensor; (**e**) schematic illustration of MI-250 gas sensor (**top**) and MI@FTO gas sensor (**bottom**) for NH_3 under N_2 condition.

The other samples (e.g., MI-300, MI-350-1h, and MI-350-3h) that contain Sn also exhibit the n-type characteristics but with a slight (or no) responsiveness to NH_3 (see Figure 9b),

even poorer than the MI@FTO, which may be due to the decomposition of the Mo cluster, thus reducing the activity site. The XRD results show that the composition of MI-300 is an extreme complex of Mo-Sn metal oxysulfur compounds, and the gas detector of MI-300 does not exhibit any selectivity for NH_3 gas. For the MI-350-1h and MI-350-3h samples, XRD results show that the main component of the product is MoS_2, which indicates that the Mo_6 cluster structure has been largely decomposed and the SnS nanocrystal has been generated together, while the macrostructure of the material changes into a porous sinter. Both MI-350-1h and MI-350-3h show a poorer selectivity for NH_3 compared to the initial MI@FTO, which may be mainly due to the decomposition of the Mo_6 cluster. During the gas sensor measurements, most of the samples, including MI-350-3h, very quickly stabilize their resistance in ambient N_2, while MI-350-1h continues to reduce its resistance in the ambient N_2, proving, on the one hand, that it is also an n-type semiconductor, and on the other hand, it has a high capacity for adsorption than selectivity. This result is consistent with the XPS Mo 3d spectrum, which shows that MI-350-1h has more Mo^{5+} components compared to MI-350-3h, meaning that it has more active sites.

It is worth noting that when the sulfurization temperature is above 400 °C, the SnO_2 layer in the FTO substrate will be destroyed and mixed into the sample (the HRTEM image of MI-400 is shown in Figure S2). Thus, the samples, which were sulfurized beyond 400 °C, were not made into a gas sensor for measurements.

Figure 9c shows the responses of MI@FTO and MI-250 based on different NH_3 gas flow rates. As the measurement circuit is at a constant voltage (0.1 V), the response calculated for the current is actually equivalent to the rate of change of the sample's resistance. The response is taken as an absolute value for the comparison; MI-250's response rate improves 3 times versus that of the MI@FTO (11% to 31%) at an NH_3 rate of 35 sccm. The increase in the response rate should be attributed to the activity sites provided by the Mo cluster [29] and the core–shell structure of MoO_3-MoS_2 [78], and probably attributed to the p–n heterojunction structure [79] between the Mo_6 cluster and MoS_2.

Based on the XRD results, the components of MI-250 can be described as a p-type Mo_x cluster ($x \leq 6$) and sulfurized n-type MoS_2 (and also MoO_x). The XPS I 3d spectrum of MI-250 also shows two clear doublets, proving that the Mo_6 cluster core is still present. Recently, it has been reported that when the Mo_6 cluster iodide is immobilized on p-type graphene (Mo_6@Graphene), this nanohybrid material exhibits a sensitivity to NO_2 gas but not NH_3 gas when made into the chemiresistive gas sensor. The response of Mo_6@Graphene to NH_3 is even lower than the response of the initial graphene to NH_3, because the NH_3 cannot exchange charges, and only few positive charges (hole) are transferred from the p-type graphene layer toward the Mo_6 cluster [80]. These results demonstrate that the sulfurized strategy is effective in enhancing the NH_3 gas response of the Mo_6 cluster iodide, probably due to the p–n heterojunction structure between the Mo_6 cluster and MoS_2.

After the sulfurization process, the resistivity of the samples shows a good linear relationship at different temperatures (see Figure S3). It means that the sulfurized Mo_6 cluster layer has good ohmic contact with the FTO electrode. Based on that, the resistance change of the gas sensor while it is exposed to the target gas can be reflected due to the negligible contact resistance at the interface. It is worth pointing out that the resistance of MI-250 and MI-300 varies very little with temperature (a small increase with temperature), which indicates that MI-250 has good stability as a gas sensor. In contrast, the resistance of MI-350, MI-350-3h, and MI-400 decreases rapidly as temperature rises, indicating that they have a high potential for future thermosensitive applications.

Figure 9d, based on Figure 9a, shows the response time and recovery time of MI@FTO and MI-250 at the NH_3 gas flow rate of 35 sccm. The response time was measured from the resistance point of the sample increasing by 10% to 90% of an end point (the maximum resistance point), while the sample was exposed to the target gas, and the recovery time was measured at the point where the resistance decreased from 90% of an end point to the 10% resistance point after the target gas was turned off. The response and recovery times for the NH_3 detection at 35 sccm by the MI@FTO are 29 s and 198 s, respectively.

In comparison, the MI-250 response and recovery times are 174 s and 254 s, respectively, both significantly lower than the performance of the MI@FTO. MI@FTO's fast response and recovery are attributed to its Mo_6 cluster core [29].

After the gas sensor measurement, the final resistance of all the samples in this 45-min long test does not go back to zero when the NH_3 gas turns off, which may be due to the fact that the sensor surface is not fully cleaned and some NH_3 is still adsorbed. This behavior may be related to operating temperature and gas flow rate.

The sulfurization process starting from the Mo_6 cluster iodides as the precursor leading to the expected MoS_2 product and their NH_3 sensing enhancement is evidence that this novel synthesis strategy is feasible. The transition of the Mo_6-cluster-iodide-based films from p-type to n-type semiconductors due to sulfurization reactions also opens up new design possibilities for future device applications, such as p–n junctions.

4. Conclusions

This study established a simple and efficient method for the synthesis of Mo cluster-MoS_2 nanocomposites, which not only demonstrates the feasibility of sulfuring Mo_6 cluster iodides as precursors to generate MoS_2, but also directly allows the synthesis of nanocomposite thin films in just one step. This study also explored the performance of Mo_6 cluster iodides and Mo cluster-MoS_2 nanocomposites as gas sensors for the first time. It was proved that the Mo_6 cluster iodide gas sensor for NH_3 at room temperature responds as a p-type semiconductor. After the sulfurization process at low temperature (250 °C), the response to NH_3 gas increased by three times while the conversion from the p-type semiconductor to n-type occurred. Our results obtained in this study show the possibilities of Mo_6 clusters and Mo-cluster-based MoS_2 material for future applications.

Supplementary Materials: The following supporting information can be downloaded at: https://www.mdpi.com/article/10.3390/nano13030478/s1, Figure S1: GIXRD pattern of FTO substrate sulfurized at different temperatures; Figure S2: HRTEM observation of MI-400 powder scratched from thin film; the same observation area is marked in the figure (**a**) HRTEM image of MI-400 with the scale bar at 100 nm; (**b**) scale bar at 10 nm; (**c**) Element mapping from HRTEM equipped with EDX device with the scale bar at 25 nm; Figure S3: Electrical measurements of the sulfurized samples at different temperatures, with a blank FTO substrate inserted at the top right as a reference.

Author Contributions: M.Z. conceived and designed the project; performed the EPD coating, sulfurization, characterization (Micro-Raman, FE-SEM, HRTEM, and XPS), gas sensor fabrication, and gas sensor measurement experiments; analyzed and interpreted the corresponding data; drafted the article; F.G. conceived and designed the project, performed the sulfurization and characterization (GIXRD) experiments, and revised the manuscript; A.R. performed the EPD coating and revised the manuscript; N.D. and S.C. conceived and designed the metal clusters chemistry and revised the manuscript; T.S. and Y.M. performed the gas sensor fabrication and gas sensor measurement experiments and revised the manuscript; T.K.N.N. performed the EPD coating and revised the manuscript; D.B. and J.-F.H. directed the project and revised the manuscript; T.U. conceived, designed, and supervised the project, and revised the manuscript. All authors have read and agreed to the published version of the manuscript.

Funding: A part of this research was funded by the ANR project NanoLetsGos grant number [ANR-22-CE09-0015-01] and the APC was waived.

Institutional Review Board Statement: Not applicable.

Informed Consent Statement: Not applicable.

Data Availability Statement: All data concerning this study are contained in the present manuscript, in previous articles or Supplementary Materials, whose references have been provided.

Acknowledgments: M. Zhang thanks the NIMS-HU joint Ph.D. program, IRL 3629 CNRS–Saint-Gobain–NIMS LINK project, and HU short-visit program for giving her the opportunity and support to stay and do cooperation research at the University of Rennes, France, from Japan before COVID-19. The authors thank Thierry Guizouarn for resistivity measurements. The authors thank the OSIRIX

Platform, from ScanMAT, UAR 2025 CNRS-Université Rennes 1 for the GIXRD investigations; Namiki Foundry, NIMS for the Micro-Raman spectroscope measurements, FE-SEM images, EDX analyses, and XPS analyses; NIMS microstructural characterization platform (NMCP) for the HRTEM images, EDX, and EELS analyses. The authors are grateful to Valérie Demange, Serge Paofaï, and Christophe Derouet from ISCR UMR6226 CNRS-UR1 for their technical assistance. ScanMAT received financial support from the European Union through the European Regional Development Fund (ERDF), the Département d'Ille et Vilaine, Rennes Métropole, and Région Bretagne (2015–2020 CPER project SCANMAT).

Conflicts of Interest: The authors declare no conflict of interest.

References

1. Fiori, G.; Bonaccorso, F.; Iannaccone, G.; Palacios, T.; Neumaier, D.; Seabaugh, A.; Banerjee, S.K.; Colombo, L. Electronics Based on Two-Dimensional Materials. *Nat. Nanotechnol.* **2014**, *9*, 768–779. [CrossRef]
2. Zeng, H.; Dai, J.; Yao, W.; Xiao, D.; Cui, X. Valley Polarization in MoS_2 Monolayers by Optical Pumping. *Nat. Nanotechnol.* **2012**, *7*, 490–493. [CrossRef]
3. Mak, K.F.; Lee, C.; Hone, J.; Shan, J.; Heinz, T.F. Atomically Thin MoS_2: A New Direct-Gap Semiconductor. *Phys. Rev. Lett.* **2010**, *105*, 136805. [CrossRef]
4. Chen, W.; Santos, E.J.G.; Zhu, W.; Kaxiras, E.; Zhang, Z. Tuning the Electronic and Chemical Properties of Monolayer MoS_2 Adsorbed on Transition Metal Substrates. *Nano Lett.* **2013**, *13*, 509–514. [CrossRef]
5. Chen, M.; Nam, H.; Wi, S.; Priessnitz, G.; Gunawan, I.M.; Liang, X. Multibit Data Storage States Formed in Plasma-Treated MoS_2 Transistors. *ACS Nano* **2014**, *8*, 4023–4032. [CrossRef]
6. Kang, J.; Liu, W.; Banerjee, K. High-Performance MoS_2 Transistors with Low-Resistance Molybdenum Contacts. *Appl. Phys. Lett.* **2014**, *104*, 093106. [CrossRef]
7. Tsai, M.-L.; Su, S.-H.; Chang, J.-K.; Tsai, D.-S.; Chen, C.-H.; Wu, C.-I.; Li, L.-J.; Chen, L.-J.; He, J.-H. Monolayer MoS_2 Heterojunction Solar Cells. *ACS Nano* **2014**, *8*, 8317–8322. [CrossRef]
8. Zhao, Y.; Ouyang, G. Thickness-Dependent Photoelectric Properties of MoS_2/Si Heterostructure Solar Cells. *Sci. Rep.* **2019**, *9*, 17381. [CrossRef]
9. Mao, J.; Wang, Y.; Zheng, Z.; Deng, D. The Rise of Two-Dimensional MoS_2 for Catalysis. *Front. Phys.* **2018**, *13*, 138118. [CrossRef]
10. Li, H.; Tsai, C.; Koh, A.L.; Cai, L.; Contryman, A.W.; Fragapane, A.H.; Zhao, J.; Han, H.S.; Manoharan, H.C.; Abild-Pedersen, F.; et al. Activating and Optimizing MoS_2 Basal Planes for Hydrogen Evolution through the Formation of Strained Sulphur Vacancies. *Nat. Mater.* **2015**, *15*, 48–53. [CrossRef]
11. Cao, Y. Roadmap and Direction toward High-Performance MoS_2 Hydrogen Evolution Catalysts. *ACS Nano* **2021**, *15*, 11014–11039. [CrossRef]
12. Akbari, E.; Jahanbin, K.; Afroozeh, A.; Yupapin, P.; Buntat, Z. Brief Review of Monolayer Molybdenum Disulfide Application in Gas Sensor. *Phys. B Condens. Matter* **2018**, *545*, 510–518. [CrossRef]
13. Liu, B.; Chen, L.; Liu, G.; Abbas, A.N.; Fathi, M.; Zhou, C. High-Performance Chemical Sensing Using Schottky-Contacted Chemical Vapor Deposition Grown Monolayer MoS_2 Transistors. *ACS Nano* **2014**, *8*, 5304–5314. [CrossRef]
14. Donarelli, M.; Ottaviano, L. 2D Materials for Gas Sensing Applications: A Review on Graphene Oxide, MoS_2, WS_2 and Phosphorene. *Sensors* **2018**, *18*, 3638. [CrossRef]
15. Kibsgaard, J.; Chen, Z.; Reinecke, B.N.; Jaramillo, T.F. Engineering the Surface Structure of MoS_2 to Preferentially Expose Active Edge Sites for Electrocatalysis. *Nat. Mater.* **2012**, *11*, 963–969. [CrossRef]
16. Li, X.; Li, T.; Ma, Y.; Wei, Q.; Qiu, W.; Guo, H.; Shi, X.; Zhang, P.; Asiri, A.M.; Chen, L.; et al. Boosted Electrocatalytic N_2 Reduction to NH_3 by Defect-Rich MoS_2 Nanoflower. *Adv. Energy Mater.* **2018**, *8*, 1801357. [CrossRef]
17. Le, D.; Rawal, T.B.; Rahman, T.S. Single-Layer MoS_2 with Sulfur Vacancies: Structure and Catalytic Application. *J. Phys. Chem. C* **2014**, *118*, 5346–5351. [CrossRef]
18. Li, L.; Qin, Z.; Ries, L.; Hong, S.; Michel, T.; Yang, J.; Salameh, C.; Bechelany, M.; Miele, P.; Kaplan, D.; et al. Role of Sulfur Vacancies and Undercoordinated Mo Regions in MoS_2 Nanosheets toward the Evolution of Hydrogen. *ACS Nano* **2019**, *13*, 6824–6834. [CrossRef]
19. Fei, H.; Guo, T.; Xin, Y.; Wang, L.; Liu, R.; Wang, D.; Liu, F.; Wu, Z. Sulfur Vacancy Engineering of MoS_2 via Phosphorus Incorporation for Improved Electrocatalytic N_2 Reduction to NH_3. *Appl. Catal. B Environ.* **2022**, *300*, 120733. [CrossRef]
20. Benck, J.D.; Hellstern, T.R.; Kibsgaard, J.; Chakthranont, P.; Jaramillo, T.F. Catalyzing the Hydrogen Evolution Reaction (HER) with Molybdenum Sulfide Nanomaterials. *ACS Catal.* **2014**, *4*, 3957–3971. [CrossRef]
21. Tsai, C.; Li, H.; Park, S.; Park, J.; Han, H.S.; Nørskov, J.K.; Zheng, X.; Abild-Pedersen, F. Electrochemical Generation of Sulfur Vacancies in the Basal Plane of MoS_2 for Hydrogen Evolution. *Nat. Commun.* **2017**, *8*, 15113. [CrossRef]
22. Kumar, R.; Zheng, W.; Liu, X.; Zhang, J.; Kumar, M. MoS_2-Based Nanomaterials for Room-Temperature Gas Sensors. *Adv. Mater. Technol.* **2020**, *5*, 1901062. [CrossRef]
23. Ramanathan, A.A. Defect Functionalization of MoS_2 Nanostructures as Toxic Gas Sensors: A Review. *IOP Conf. Ser. Mater. Sci. Eng.* **2018**, *305*, 012001. [CrossRef]

24. Burman, D.; Ghosh, R.; Santra, S.; Ray, S.K.; Guha, P.K. Role of Vacancy Sites and UV-Ozone Treatment on Few Layered MoS_2 nanoflakes for Toxic Gas Detection. *Nanotechnology* **2017**, *28*, 435502. [CrossRef]
25. Xie, J.; Zhang, H.; Li, S.; Wang, R.; Sun, X.; Zhou, M.; Zhou, J.; Lou, X.W.D.; Xie, Y. Defect-Rich MoS_2 Ultrathin Nanosheets with Additional Active Edge Sites for Enhanced Electrocatalytic Hydrogen Evolution. *Adv. Mater.* **2013**, *25*, 5807–5813. [CrossRef]
26. Zhang, Z.; Dong, Y.; Sun, H.; Liu, G.; Liu, S.; Yang, X. Defect-Rich 2D Reticulated MoS_2 Monolayers: Facile Hydrothermal Preparation and Marvellous Photoelectric Properties. *J. Taiwan Inst. Chem. Eng.* **2019**, *101*, 221–230. [CrossRef]
27. Syari'ati, A.; Kumar, S.; Zahid, A.; El Yumin, A.A.; Ye, J.; Rudolf, P. Photoemission Spectroscopy Study of Structural Defects in Molybdenum Disulfide (MoS_2) Grown by Chemical Vapor Deposition (CVD). *Chem. Commun.* **2019**, *55*, 10384–10387. [CrossRef]
28. Young, B.T.; Pathan, M.A.K.; Jiang, T.; Le, D.; Marrow, N.; Nguyen, T.; Jordan, C.E.; Rahman, T.S.; Popolan-Vaida, D.M.; Vaida, M.E. Catalytic C_2H_2 Synthesis via Low Temperature CO Hydrogenation on Defect-Rich 2D-MoS_2 and 2D-MoS_2 Decorated with Mo Clusters. *J. Chem. Phys.* **2020**, *152*, 074706. [CrossRef]
29. Zhang, Z.; Xu, X. Mechanistic Study on Enhanced Electrocatalytic Nitrogen Reduction Reaction by Mo Single Clusters Supported on MoS_2. *ACS Appl. Mater. Interfaces* **2022**, *14*, 28900–28910. [CrossRef]
30. Huang, W.; Wang, X.; Ji, X.; Zhang, Z.; Jin, C. In-Situ Fabrication of Mo_6S_6-Nanowire-Terminated Edges in Monolayer Molybdenum Disulfide. *Nano Res.* **2018**, *11*, 5849–5857. [CrossRef]
31. Wang, X.-W.; Hou, L.-F.; Huang, W.; Ren, X.-B.; Ji, W.; Jin, C.-H. Mass Transport Induced Structural Evolution and Healing of Sulfur Vacancy Lines and Mo Chain in Monolayer MoS_2. *Rare Met.* **2021**, *41*, 333–341. [CrossRef]
32. Viršek, M.; Novak, N.; Filipič, C.; Kump, P.; Remškar, M.; Kutnjak, Z. Transport Properties in MoS_2 Selective Morphology System. *J. Appl. Phys.* **2012**, *112*, 103710. [CrossRef]
33. Viršek, M.; Krause, M.; Kolitsch, A.; Mrzel, A.; Iskra, I.; Škapin, S.D.; Remškar, M. The Transformation Pathways of $Mo_6S_2I_8$ Nanowires into Morphology-Selective MoS_2 Nanostructures. *J. Phys. Chem. C* **2010**, *114*, 6458–6463. [CrossRef]
34. Chevrel, R.; Sergent, M.; Prigent, J. Sur de Nouvelles Phases Sulfurées Ternaires Du Molybdène. *J. Solid State Chem.* **1971**, *3*, 515–519. [CrossRef]
35. Perrin, A.; Perrin, C. The Molybdenum and Rhenium Octahedral Cluster Chalcohalides in Solid State Chemistry: From Condensed to Discrete Cluster Units. *Comptes Rendus Chim.* **2012**, *15*, 815–836. [CrossRef]
36. Fedorov, V. Metal Clusters. As They Were Born in Siberia. *J. Clust. Sci.* **2014**, *26*, 3–15. [CrossRef]
37. Vorotnikova, N.A.; Vorotnikov, Y.A.; Novozhilov, I.N.; Syrokvashin, M.M.; Nadolinny, V.A.; Kuratieva, N.V.; Benoit, D.M.; Mironov, Y.V.; Walton, R.I.; Clarkson, G.J.; et al. 23-Electron Octahedral Molybdenum Cluster Complex $[\{Mo_6I_8\}Cl_6]^-$. *Inorg. Chem.* **2017**, *57*, 811–820. [CrossRef]
38. Nguyen, N.T.K.; Lebastard, C.; Wilmet, M.; Dumait, N.; Renaud, A.; Cordier, S.; Ohashi, N.; Uchikoshi, T.; Grasset, F. A Review on Functional Nanoarchitectonics Nanocomposites Based on Octahedral Metal Atom Clusters (Nb_6, Mo_6, Ta_6, W_6, Re_6): Inorganic 0D and 2D Powders and Films. *Sci. Technol. Adv. Mater.* **2022**, *23*, 547–578. [CrossRef]
39. Costuas, K.; Garreau, A.; Bulou, A.; Fontaine, B.; Cuny, J.; Gautier, R.; Mortier, M.; Molard, Y.; Duvail, J.-L.; Faulques, E.; et al. Combined Theoretical and Time-Resolved Photoluminescence Investigations of $[Mo_6Br^i{}_8Br^a{}_6]^{2-}$ Metal Cluster Units: Evidence of Dual Emission. *Phys. Chem. Chem. Phys.* **2015**, *17*, 28574–28585. [CrossRef]
40. Sokolov, M.N.; Mihailov, M.A.; Peresypkina, E.V.; Brylev, K.A.; Kitamura, N.; Fedin, V.P. Highly Luminescent Complexes $[Mo_6X_8(N\text{-}C_3F_7COO)_6]^{2-}$ (X = Br, I). *Dalton Trans.* **2011**, *40*, 6375. [CrossRef]
41. Dierre, B.; Costuas, K.; Dumait, N.; Paofai, S.; Amela-Cortes, M.; Molard, Y.; Grasset, F.; Cho, Y.; Takahashi, K.; Ohashi, N.; et al. Mo_6 Cluster-Based Compounds for Energy Conversion Applications: Comparative Study of Photoluminescence and Cathodoluminescence. *Sci. Technol. Adv. Mater.* **2017**, *18*, 458–466. [CrossRef] [PubMed]
42. Dybtsev, D.; Serre, C.; Schmitz, B.; Panella, B.; Hirscher, M.; Latroche, M.; Llewellyn, P.L.; Cordier, S.; Molard, Y.; Haouas, M.; et al. Influence of $[Mo_6Br_8F_6]^{2-}$ Cluster Unit Inclusion within the Mesoporous Solid MIL-101 on Hydrogen Storage Performance. *Langmuir* **2010**, *26*, 11283–11290. [CrossRef] [PubMed]
43. Barras, A.; Das, M.R.; Devarapalli, R.R.; Shelke, M.V.; Cordier, S.; Szunerits, S.; Boukherroub, R. One-Pot Synthesis of Gold Nanoparticle/Molybdenum Cluster/Graphene Oxide Nanocomposite and Its Photocatalytic Activity. *Appl. Catal. B Environ.* **2013**, *130–131*, 270–276. [CrossRef]
44. Nguyen, N.T.K.; Renaud, A.; Dierre, B.; Bouteille, B.; Wilmet, M.; Dubernet, M.; Ohashi, N.; Grasset, F.; Uchikoshi, T. Extended Study on Electrophoretic Deposition Process of Inorganic Octahedral Metal Clusters: Advanced Multifunctional Transparent Nanocomposite Thin Films. *Bull. Chem. Soc. Jpn.* **2018**, *91*, 1763–1774. [CrossRef]
45. Renaud, A.; Jouan, P.-Y.; Dumait, N.; Ababou-Girard, S.; Barreau, N.; Uchikoshi, T.; Grasset, F.; Jobic, S.; Cordier, S. Evidence of the Ambipolar Behavior of Mo_6 Cluster Iodides in All-Inorganic Solar Cells: A New Example of Nanoarchitectonic Concept. *ACS Appl. Mater. Interfaces* **2021**, *14*, 1347–1354. [CrossRef] [PubMed]
46. Guy, K.; Tessier, F.; Kaper, H.; Grasset, F.; Dumait, N.; Demange, V.; Nishio, M.; Matsushita, Y.; Matsui, Y.; Takei, T.; et al. Original Synthesis of Molybdenum Nitrides Using Metal Cluster Compounds as Precursors: Applications in Heterogeneous Catalysis. *Chem. Mater.* **2020**, *32*, 6026–6034. [CrossRef]
47. Zhang, M.Q.; Grasset, F.; Dumait, N.; Cordier, S.; Shimada, T.; Uchikoshi, T. Effect of Sulfurization Process on Octahedral Molybdenum Cluster from Mo_6 Cluster to MoS_2 Nanosheet. *Key Eng. Mater.* **2021**, *904*, 334–338. [CrossRef]

48. Saito, G.; Hosoda, H.; Yoshida, Y.; Hagiwara, J.; Nishimura, K.; Yamochi, H.; Otsuka, A.; Hiramatsu, T.; Shimazaki, Y.; Kirakci, K.; et al. Synthesis and Properties of Charge-Transfer Solids with Cluster Units $[Mo_6X_{14}]^{2-}$ (X = Br, I). *J. Mater. Chem.* **2012**, *22*, 19774. [CrossRef]
49. Kirakci, K.; Cordier, S.; Perrin, C. Synthesis and Characterization of $Cs_2Mo_6X_{14}$ (X = Br or I) Hexamolybdenum Cluster Halides: Efficient Mo_6 Cluster Precursors for Solution Chemistry Syntheses. *Z. Anorg. Und Allg. Chem.* **2005**, *631*, 411–416. [CrossRef]
50. Nguyen, T.K.N.; Grasset, F.; Dierre, B.; Matsunaga, C.; Cordier, S.; Lemoine, P.; Ohashi, N.; Uchikoshi, T. Fabrication of Transparent Thin Film of Octahedral Molybdenum Metal Clusters by Electrophoretic Deposition. *ECS J. Solid State Sci. Technol.* **2016**, *5*, R178–R186. [CrossRef]
51. Renaud, A.; Nguyen, T.K.N.; Grasset, F.; Raissi, M.; Guillon, V.; Delabrouille, F.; Dumait, N.; Jouan, P.-Y.; Cario, L.; Jobic, S.; et al. Preparation by Electrophoretic Deposition of Molybdenum Iodide Cluster-Based Functional Nanostructured Photoelectrodes for Solar Cells. *Electrochim. Acta* **2019**, *317*, 737–745. [CrossRef]
52. Akram, H.; Mateos-Pedrero, C.; Gallegos-Suarez, E.; Chafik, T.; Guerrero-Ruiz, A.; Rodríguez-Ramos, I. Effect of Surfactant Concentration on the Morphology of Mo_xS_y Nanoparticles Prepared by a Solvothermal Route. *Green Process. Synth.* **2017**, *6*, 161–171. [CrossRef]
53. Polivtseva, S.; Acik, I.O.; Katerski, A.; Mere, A.; Mikli, V.; Krunks, M. Spray Pyrolysis Deposition of Sn_xS_y Thin Films. *Energy Procedia* **2014**, *60*, 156–165. [CrossRef]
54. Kaidi, Z.; Boulanger, C.; Lecuire, J.M.; Lemée, N.; Guilloux-Viry, M.; Perrin, A. Ternary Molybdenum Cluster Sulfides: Electrochemical and Chemical Behavior of in Situ Pulsed Laser Deposited Thin Films. *Solid State Sci.* **1999**, *1*, 623–635. [CrossRef]
55. Genuit, D.; Bezverkhyy, I.; Afanasiev, P. Solution Preparation of the Amorphous Molybdenum Oxysulfide $MoOS_2$ and Its Use for Catalysis. *J. Solid State Chem.* **2005**, *178*, 2759–2765. [CrossRef]
56. Liu, G.; Li, Z.; Hasan, T.; Chen, X.; Zheng, W.; Feng, W.; Jia, D.; Zhou, Y.; Hu, P. Vertically Aligned Two-Dimensional SnS_2 Nanosheets with a Strong Photon Capturing Capability for Efficient Photoelectrochemical Water Splitting. *J. Mater. Chem. A* **2017**, *5*, 1989–1995. [CrossRef]
57. Burton, L.A.; Colombara, D.; Abellon, R.D.; Grozema, F.C.; Peter, L.M.; Savenije, T.J.; Dennler, G.; Walsh, A. Synthesis, Characterization, and Electronic Structure of Single-Crystal SnS, Sn_2S_3, and SnS_2. *Chem. Mater.* **2013**, *25*, 4908–4916. [CrossRef]
58. Harada, K.; Nguyen, T.K.N.; Grasset, F.; Comby-Zerbino, C.; MacAleese, L.; Chirot, F.; Dugourd, P.; Dumait, N.; Cordier, S.; Ohashi, N.; et al. Light-Dependent Ionic-Electronic Conduction in an Amorphous Octahedral Molybdenum Cluster Thin Film. *NPG Asia Mater.* **2022**, *14*, 21. [CrossRef]
59. Chen, Z.; Cummins, D.; Reinecke, B.N.; Clark, E.; Sunkara, M.K.; Jaramillo, T.F. Core–Shell MoO_3–MoS_2 Nanowires for Hydrogen Evolution: A Functional Design for Electrocatalytic Materials. *Nano Lett.* **2011**, *11*, 4168–4175. [CrossRef]
60. Saito, N.; Cordier, S.; Lemoine, P.; Ohsawa, T.; Wada, Y.; Grasset, F.; Cross, J.S.; Ohashi, N. Lattice and Valence Electronic Structures of Crystalline Octahedral Molybdenum Halide Clusters-Based Compounds, $Cs_2[Mo_6X_{14}]$ (X = Cl, Br, I), Studied by Density Functional Theory Calculations. *Inorg. Chem.* **2017**, *56*, 6234–6243. [CrossRef]
61. Rodenes, M.; Gonell, F.; Martín, S.; Corma, A.; Sorribes, I. Molecularly Engineering Defective Basal Planes in Molybdenum Sulfide for the Direct Synthesis of Benzimidazoles by Reductive Coupling of Dinitroarenes with Aldehydes. *JACS Au* **2022**, *2*, 601–612. [CrossRef] [PubMed]
62. Fominski, V.; Demin, M.; Nevolin, V.; Fominski, D.; Romanov, R.; Gritskevich, M.; Smirnov, N. Reactive Pulsed Laser Deposition of Clustered-Type MoS_x (X ~ 2, 3, and 4) Films and Their Solid Lubricant Properties at Low Temperature. *Nanomaterials* **2020**, *10*, 653. [CrossRef] [PubMed]
63. Lee, C.-H.; Lee, S.; Lee, Y.-K.; Jung, Y.C.; Ko, Y.-I.; Lee, D.C.; Joh, H.-I. Understanding the Origin of Formation and Active Sites for Thiomolybdate $[Mo_3S_{13}]^{2-}$ Clusters as Hydrogen Evolution Catalyst through the Selective Control of Sulfur Atoms. *ACS Catal.* **2018**, *8*, 5221–5227. [CrossRef]
64. Seo, B.; Jung, G.Y.; Lee, S.J.; Baek, D.S.; Sa, Y.J.; Ban, H.W.; Son, J.S.; Park, K.; Kwak, S.K.; Joo, S.H. Monomeric MoS_4^{2-}-Derived Polymeric Chains with Active Molecular Units for Efficient Hydrogen Evolution Reaction. *ACS Catal.* **2019**, *10*, 652–662. [CrossRef]
65. Pritzi, M.; Pascher, T.F.; Grutza, M.-L.; Kurz, P.; Ončák, M.; Beyer, M.K. Decomposition of Halogenated Molybdenum Sulfide Dianions $[Mo_3S_7X_6]^{2-}$ (X = Cl, Br, I). *J. Am. Soc. Mass Spectrom.* **2022**, *33*, 1753–1760. [CrossRef]
66. de Jong, A.M.; Borg, H.J.; van IJzendoorn, L.J.; Soudant, V.G.F.M.; de Beer, V.H.J.; van Veen, J.A.R.; Niemantsverdriet, J.W. Sulfidation Mechanism by Molybdenum Catalysts Supported on Silica/Silicon(100) Model Support Studied by Surface Spectroscopy. *J. Phys. Chem.* **1993**, *97*, 6477–6483. [CrossRef]
67. Ghosh, R.N.; Baker, G.L.; Ruud, C.; Nocera, D.G. Fiber-Optic Oxygen Sensor Using Molybdenum Chloride Cluster Luminescence. *Appl. Phys. Lett.* **1999**, *75*, 2885–2887. [CrossRef]
68. Ghosh, R.N.; Askeland, P.A.; Kramer, S.; Loloee, R. Optical Dissolved Oxygen Sensor Utilizing Molybdenum Chloride Cluster Phosphorescence. *Appl. Phys. Lett.* **2011**, *98*, 221103. [CrossRef]
69. Khazieva, A.; Kholin, K.; Nizameev, I.; Brylev, K.; Kashnik, I.; Voloshina, A.; Lyubina, A.; Gubaidullin, A.; Daminova, A.; Petrov, K.; et al. Surface Modification of Silica Nanoparticles by Hexarhenium Anionic Cluster Complexes for PH-Sensing and Staining of Cell Nuclei. *J. Colloid Interface Sci.* **2021**, *594*, 759–769. [CrossRef]

70. Elistratova, J.; Mikhailov, M.; Burilov, V.; Babaev, V.; Rizvanov, I.; Mustafina, A.; Abramov, P.; Sokolov, M.; Konovalov, A.; Fedin, V. Supramolecular Assemblies of Triblock Copolymers with Hexanuclear Molybdenum Clusters for Sensing Antibiotics in Aqueous Solutions via Energy Transfer. *RSC Adv.* **2014**, *4*, 27922–27930. [CrossRef]
71. Nguyen, T.K.N.; Dumait, N.; Grasset, F.; Cordier, S.; Berthebaud, D.; Matsui, Y.; Ohashi, N.; Uchikoshi, T. Zn–al Layered Double Hydroxide Film Functionalized by a Luminescent Octahedral Molybdenum Cluster: Ultraviolet–Visible Photoconductivity Response. *ACS Appl. Mater. Interfaces* **2020**, *12*, 40495–40509. [CrossRef] [PubMed]
72. Cao, J.; Chen, Q.; Wang, X.; Zhang, Q.; Yu, H.-D.; Huang, X.; Huang, W. Recent Development of Gas Sensing Platforms Based on 2D Atomic Crystals. *Research* **2021**, *2021*, 9863038. [CrossRef] [PubMed]
73. Late, D.J.; Huang, Y.-K.; Liu, B.; Acharya, J.; Shirodkar, S.N.; Luo, J.; Yan, A.; Charles, D.; Waghmare, U.V.; Dravid, V.P.; et al. Sensing Behavior of Atomically Thin-Layered MoS_2 Transistors. *ACS Nano* **2013**, *7*, 4879–4891. [CrossRef] [PubMed]
74. Wang, Y.; Duan, L.; Deng, Z.; Liao, J. Electrically Transduced Gas Sensors Based on Semiconducting Metal Oxide Nanowires. *Sensors* **2020**, *20*, 6781. [CrossRef]
75. Shang, H.; Wang, T.; Zhang, W. Sulfur Vacancy Formation at Different MoS_2 Edges during Hydrodesulfurization Process: A DFT Study. *Chem. Eng. Sci.* **2019**, *195*, 208–217. [CrossRef]
76. Yang, L.; Majumdar, K.; Liu, H.; Du, Y.; Wu, H.; Hatzistergos, M.; Hung, P.Y.; Tieckelmann, R.; Tsai, W.; Hobbs, C.; et al. Chloride Molecular Doping Technique on 2D Materials: WS_2 and MoS_2. *Nano Lett.* **2014**, *14*, 6275–6280. [CrossRef]
77. Murugan, P.; Kumar, V.; Kawazoe, Y.; Ota, N. Assembling Nanowires from Mo−S Clusters and Effects of Iodine Doping on Electronic Structure. *Nano Lett.* **2007**, *7*, 2214–2219. [CrossRef]
78. Yuan, Z.; Liu, Y.; Zhang, J.; Meng, F.; Zhang, H. Rose-like MoO_3/MoS_2/RGO Low-Temperature Ammonia Sensors Based on Multigas Detection Methods. *IEEE Trans. Instrum. Meas.* **2021**, *70*, 1–9. [CrossRef]
79. Kim, Y.; Lee, S.; Song, J.; Ko, K.Y.; Woo, W.J.; Lee, S.W.; Park, M.; Lee, H.; Lee, Z.; Choi, H.; et al. 2D Transition Metal Dichalcogenide Heterostructures for P- and N-Type Photovoltaic Self-Powered Gas Sensor. *Adv. Funct. Mater.* **2020**, *30*, 2003360. [CrossRef]
80. Casanova-Chafer, J.; Garcia-Aboal, R.; Atienzar, P.; Feliz, M.; Llobet, E. Octahedral Molybdenum Iodide Clusters Supported on Graphene for Resistive and Optical Gas Sensing. *ACS Appl. Mater. Interfaces* **2022**, *14*, 57122–57132. [CrossRef]